Variational Feature Extraction in Scientific Visualization – Additional Experiments

NICO DASSLER and TOBIAS GÜNTHER, Friedrich-Alexander-Universität Erlangen-Nürnberg, Germany

ACM Reference Format:
Nico Daßler and Tobias Günther. 2024. Variational Feature Extraction in Scientific Visualization – Additional Experiments. *ACM Trans. Graph.* 43, 4, Article 109 (July 2024), 3 pages. https://doi.org/10.1145/3658219

This document contains further experiments. In the following, we provide further feature definitions for the modeling of Jacobi sets in Section 1, and for wind wake centerlines in Section 2. Afterwards, we elaborate on the convergence behavior in Section 3, where we examine the reduction of the functional derivatives, the distance to ground truths, and the dependence on the seed point.

1 JACOBI SETS

1.1 Definition

In Morse theory, a branch of differential topology, the relationships of two Morse functions can be studied using Jacobi sets [Edelsbrunner and Harer 2002; Klötzl et al. 2022]. A Jacobi set is defined for two m-dimensional scalar fields $s_1(\mathbf{y}), s_2(\mathbf{y}) : \mathbb{R}^m \to \mathbb{R}$ as the union of all locations at which the two gradient fields align:

$$\{\mathbf{y} \;:\; \nabla s_1(\mathbf{y}) \parallel \nabla s_2(\mathbf{y})\}. \tag{1}$$

For two 3-dimensional scalar fields $s_1(\mathbf{y}), s_2(\mathbf{y}) : \mathbb{Y} \to \mathbb{R}$, we define a 1-dimensional Jacobi set $\big(f_1(x), \ldots, f_3(x)\big)^{\mathrm{T}}$ variationally as minimizer using the following feature term and its functional derivative:

$$\mathcal{M}^j = \frac{1}{2} \left\| \nabla s_1(\mathbf{f}(x)) \times \nabla s_2(\mathbf{f}(x)) \right\|^2, \tag{2}$$

$$\frac{\delta \mathcal{M}^p}{\delta \mathbf{f}(x)} = (\nabla s_1 \times \nabla s_2)^{\mathrm{T}} \cdot \begin{pmatrix} (\frac{\partial \nabla s_1}{\partial f_1} \times \nabla s_2 + \nabla s_1 \times \frac{\partial \nabla s_2}{\partial f_1})^{\mathrm{T}} \\ \vdots \\ (\frac{\partial \nabla s_1}{\partial f_m} \times \nabla s_2 + \nabla s_1 \times \frac{\partial \nabla s_2}{\partial f_m})^{\mathrm{T}} \end{pmatrix}^{\mathrm{T}}. \tag{3}$$

In Eq. (3), we dropped the dependencies for brevity, i.e., $\nabla s_1 := \nabla s_1(\mathbf{f}(x))$ and $\nabla s_2 := \nabla s_2(\mathbf{f}(x))$. To treat 2D scalar fields, the third component of the gradients ∇s_1 and ∇s_2 is set to zero.

1.2 Experiment

For demonstrative purposes, we treat the two velocity components (u, v) of a two-dimensional flow around a cylinder [Günther et al. 2017] as scalar functions. Thus, given the two 2-dimensional scalar fields $u(\mathbf{y}), v(\mathbf{y}) : \mathbb{Y} \to \mathbb{R}$, we extract a smooth 1-dimensional Jacobi set $\mathbf{f}(x) = \big(f_1(x), f_2(x)\big)^{\mathrm{T}}$ by inserting the velocity field components into Eq. (2), which gives:

$$\mathcal{L}^{\text{jacobi}} = \underbrace{\frac{1}{2} \left\| \frac{\partial u(\mathbf{f})}{\partial y_1} \frac{\partial v(\mathbf{f})}{\partial y_2} - \frac{\partial u(\mathbf{f})}{\partial y_2} \frac{\partial v(\mathbf{f})}{\partial y_1} \right\|^2}_{\text{Jacobi set}} + \underbrace{\frac{\lambda_s}{2} \|\nabla \mathbf{f}(x)\|^2}_{\text{smoothness}}. \tag{4}$$

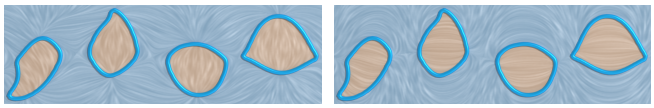

$\nabla u(\mathbf{y})$ $\nabla v(\mathbf{y})$

Fig. 1. Results of the Jacobi set extraction from the scalar components of a 2-dimensional vector field. The Jacobi set (blue line) shows all locations, at which the gradient of the u component (shown as LIC on the left) and the gradient of the v component (shown as LIC on the right) are aligned. The color in the background shows the sign of the scalar quantity in which the Jacobi set arises as isocontour with isovalue zero.

The Jacobi set term is what the 3D expression in Eq. (2) simplifies to for a 2D field, which is the last component of the 3D cross product. Fig. 1 displays the result. The left image shows the gradient of u with a line integral convolution [Cabral and Leedom 1993], while the right image shows the gradient of v. The color in the background depicts the third component of the cross product, i.e., the signed term in the Jacobi set norm of Eq. (4). The blue lines are the result of our variational feature extraction for $\lambda_s = 10^5$, using gradient descent (step size $h = 10^{-2}$) for growing and subsequent refinement. The blue lines separate regions of equal sign in the third cross product component well, which is the desired result. In this example, we extracted *closed* feature curves. Thus, the growing automatically terminates and closes the feature curve when the end points of the curve are close enough to each other.

2 WIND ENGINEERING

2.1 Definition

Wind engineering is concerned with the efficient operation of clean energy sources. For wind farms, a key driver for the efficiency of a turbine is the wind force acting on the blades. In a larger array of wind turbines, the individual turbines produce wake corridors with reduced wind magnitude, in which another turbine will experience a reduced efficiency [Barthelmie and Jensen 2010]. In wind engineering, assumptions about velocity profiles [Vollmer et al. 2016] or automatic thresholding methods [Krutova et al. 2022] have been used, which assume that multiple wind wakes do not interfere. To model domain knowledge about the expected feature direction, we add a regularizer that orientates the feature curve ($n = 1$) along a

Authors' address: Nico Daßler, nico.dassler@fau.de; Tobias Günther, tobias.guenther@fau.de, Friedrich-Alexander-Universität Erlangen-Nürnberg, Cauerstr. 11, Erlangen, Bavaria, 91058, Germany.

0730-0301/2024/7-ART109
https://doi.org/10.1145/3658219

given tangent direction $\mathbf{v}(x) : \mathbb{X} \rightarrow \mathbb{R}^m$:

$$\Gamma^o = \frac{1}{2}\|\mathbf{v}(x) - \nabla\mathbf{f}(x)\|^2, \qquad \frac{\delta\Gamma^o}{\delta\mathbf{f}} = (\nabla\mathbf{v}(x) - \nabla^2\mathbf{f}(x))^{\mathrm{T}}. \tag{5}$$

This formulation is the building block behind Poisson-based vector field exploration tools [Esturo et al. 2013]. As with flow alignment, the orientation can be enforced with a Neumann boundary condition $\nabla\mathbf{f}(x_0) = \mathbf{v}(x_0)$ at point $x_0 \in \mathbb{X}$ along the curve.

2.2 Experiment

Formally, let $\mathbf{v}(\mathbf{y})$ be the wind vector field and let $s(\mathbf{y})$ be its magnitude field, i.e., $s(\mathbf{y}) = \|\mathbf{v}(\mathbf{y})\|$. Further, we let $\mathbf{v}(x)$ be the constant downstream direction of the flow. We define the wind wake centerlines variationally as minimizer of the following Lagrangian:

$$\mathcal{L}^{\text{wake}} = \underbrace{\frac{1}{2}\|\nabla s(\mathbf{f}(x)) \times \mathbf{c}_1(\mathbf{f}(x))\|^2}_{\text{valley line}} + \underbrace{\frac{\lambda_o}{2}\|\mathbf{v}(x) - \nabla\mathbf{f}(x)\|^2}_{\text{orientation}}, \tag{6}$$

Fig. 2 shows the results of a wind wake corridor extraction in a Lattice-Boltzmann simulation [Schottenhamml et al. 2022]. Blue regions indicate a low velocity magnitude.

Multi-Scale Extraction. The wake of the wind turbine is turbulent, which complicates the extraction of a long valley line. To improve the convergence to a better optimum, we followed a multi-scale approach that optimizes on the low frequency band of the field first. In Figs. 2(a)-(c), we successively extracted the wind wake from a less and less smoothed field, using the solution of the previous smoother level as next initial guess. In comparison, the direct variational extraction without multi-scale approach in Fig. 2(d) is locally stuck in a suboptimal path. This is another example for the importance of finding a suitable initial guess to start from. Optimizations were done using Adam (learning rate $h = 10^{-4}$) with our refine method as described above. The first extraction was seeded from a straight line. For all extractions, we used $\lambda_o = 10^6$ as the orientation weight.

3 CONVERGENCE

Vanishing Functional Derivative. The gradient-based optimization of the variational problem requires a suitable setting of numerical parameters, such as the step size, and the number of iterations. For the parameter selection, it is helpful to visualize the reduction of the functional derivative over time, which is expected to vanish to zero as the feature converges. Fig. 3 shows the convergence plots for the delta wing (aerodynamics) in (a), the Earth mantle (geophysics) in (b), the ocean eddies (oceanography) in (c), and the extremal surface in (d). In all cases, convergence can be observed.

Convergence to Ground Truth. For the extremal surface in Fig. 4, an exact ground truth surface is known by construction. In the plot, we visualize the average vertex error for an increasing number of refinement iterations. The residual error decreases, as the surface converges from its initial guess to the ground truth. Another ground truth comparison in the following paragraph, as well.

Seed Sensitivity. Since the tensor coreline example is an analytic data set without regularizer, the ground truth tensor coreline is known. In Fig. 5, we plot the residual of the refinement process after

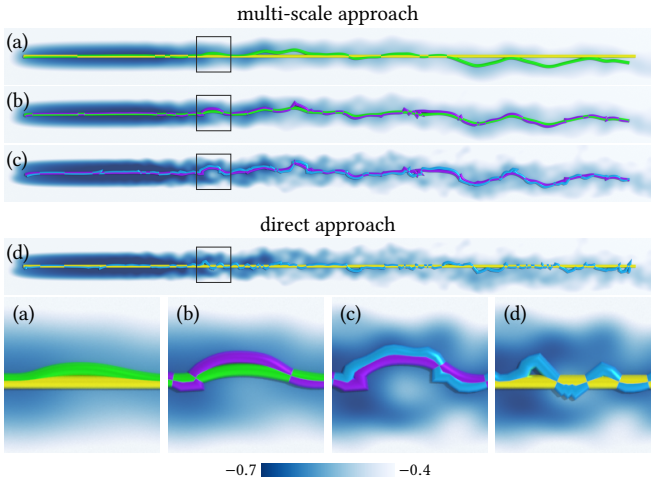

Fig. 2. In the turbulent wake behind a wind turbine, the eastward wake centerline is extracted as magnitude valley line. (a)-(c) shows a variational multi-scale extraction, while (d) shows the direct extraction. (a) extracts the green line from the yellow seed line in a smoothed field. (b) takes the green line from above and extracts the purple line in a less smoothed field. (c) takes the purple line as input and extracts the final blue line in the unsmoothed field. For comparison, (d) tries to extract the valley line immediately in the unsmoothed field from the yellow seed line, which is not successful.

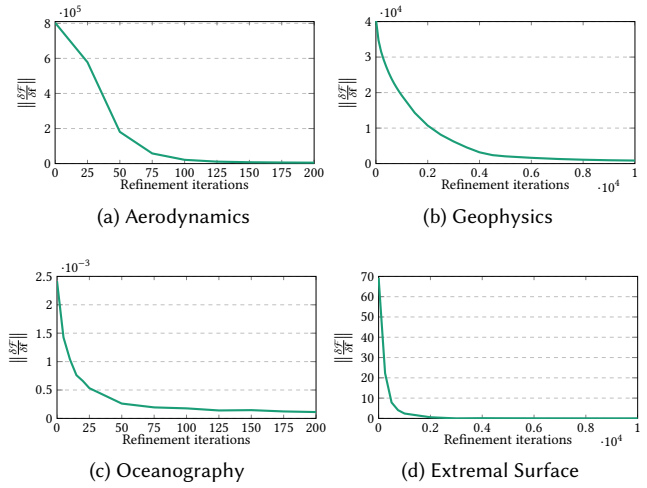

Fig. 3. Plots of the gradient norm, i.e., the norm of the functional derivative $\|\delta\mathcal{F}[\mathbf{f}(\mathbf{x})]/\delta\mathbf{f}\|$, during the refinement process. For all data sets, the gradient norm decreases as expected while the feature curves/surfaces converge.

the first growth step for three different 6D seed points $(1, 0, 0, 1, 1, 0)$ (green), $(0.5, 0, 0, 1, 1, 0)$ (orange), and $(0.3, 0, 0, 1, 1, 0)$ (purple). The refinement converges onto the coreline, although this happens at a slow rate. When beginning at a spatial distance of more than 1.1, the refinement is unable to converge to the tensor coreline and the method fails, which underlines that a suitable seed point is required.

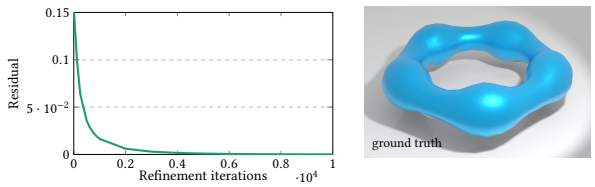

Fig. 4. Residual plot of our ridge surface extraction, showing the convergence towards the ground truth after a sufficient number of iterations.

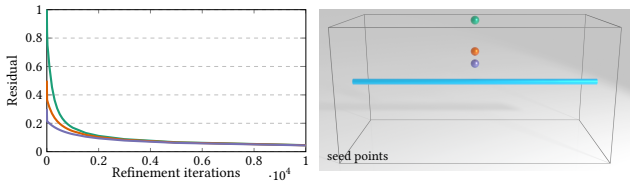

Fig. 5. Here, we study the seed point sensitivity at the tensor coreline example using three different seed points (right image). Due to the symmetry of the data set, the result is radially symmetric for other seed points at the same distance from the coreline. Residual plots (left image) show the convergence rate for an increasing number of refinement iterations. The optimization used gradient descent. The computation converged for all three seed points. At a larger distance, the optimization fails.

REFERENCES

Rebecca Jane Barthelmie and LE Jensen. 2010. Evaluation of wind farm efficiency and wind turbine wakes at the Nysted offshore wind farm. *Wind Energy* 13, 6 (2010), 573–586. https://doi.org/10.1002/we.408

Brian Cabral and Leith Leedom. 1993. Imaging Vector Fields Using Line Integral Convolution. *Computer Graphics (Proc. SIGGRAPH)* 27 (1993), 263–272. https://doi.org/10.1145/166117.166151

Herbert Edelsbrunner and John Harer. 2002. Jacobi sets of multiple Morse functions. *Foundations of computational mathematics, Minneapolis* 8 (2002), 35–57. https://doi.org/10.1017/CBO9781139106962.003

Janick Martinez Esturo, Maik Schulze, Christian Rössl, and Holger Theisel. 2013. Poisson-based tools for flow visualization. In *2013 IEEE Pacific Visualization Symposium (PacificVis)*. IEEE, IEEE, Sydney, NSW, Australia, 241–248. https://doi.org/10.1109/PacificVis.2013.6596151

Tobias Günther, Markus Gross, and Holger Theisel. 2017. Generic Objective Vortices for Flow Visualization. *ACM Transactions on Graphics (Proc. SIGGRAPH)* 36, 4 (2017), 1–11. https://doi.org/10.1145/3072959.3073684

Daniel Klötzl, Tim Krake, Youjia Zhou, Ingrid Hotz, Bei Wang, and Daniel Weiskopf. 2022. Local bilinear computation of Jacobi sets. *The Visual Computer* 38, 9-10 (2022), 3435–3448. https://doi.org/10.1007/s00371-022-02557-4

Maria Krutova, Mostafa Bakhoday-Paskyabi, Joachim Reuder, and Finn Gunnar Nielsen. 2022. Development of an automatic thresholding method for wake meandering studies and its application to the data set from scanning wind lidar. *Wind Energy Science* 7, 2 (2022), 849–873. https://doi.org/10.5194/wes-7-849-2022

Helen Schottenhamml, Ani Anciaux-Sedrakian, Frédéric Blondel, Adria Borras-Nadal, Pierre-Antoine Joulin, and Ulrich Rüde. 2022. Evaluation of a lattice Boltzmann-based wind-turbine actuator line model against a Navier-Stokes approach. *Journal of Physics: Conference Series* 2265, 2 (2022), 022027. https://doi.org/10.1088/1742-6596/2265/2/022027

Lukas Vollmer, Gerald Steinfeld, Detlev Heinemann, and Martin Kühn. 2016. Estimating the wake deflection downstream of a wind turbine in different atmospheric stabilities: an LES study. *Wind Energy Science* 1, 2 (2016), 129–141. https://doi.org/10.5194/wes-1-129-2016